

A Computational Study on Choline Benzoate and Choline Salicylate Ionic Liquids in the Pure State and After CO₂ Adsorption

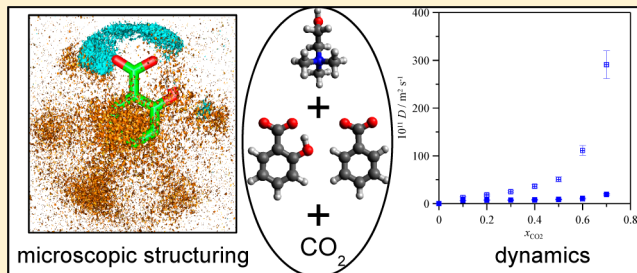
Santiago Aparicio*,† and Mert Atilhan‡

†Department of Chemistry, University of Burgos, 09001 Burgos, Spain

‡Chemical Engineering Department, Qatar University, Doha, Qatar

S Supporting Information

ABSTRACT: Choline-based ionic liquids show very adequate environmental, toxicological, and economical profiles for their application in many different technological areas. We report in this work a computational study on the properties of choline benzoate and choline salicylate ionic liquids, as representatives of this family of compounds, in the pure state and after CO₂ adsorption. Quantum chemistry calculations using the density functional theory approach for ionic pairs and ions, CO₂ pairs, were carried out, and the results analyzed using natural bond orbital and atoms in a molecule approaches. Classical molecular dynamics simulations of ionic liquids were done as a function of pressure, temperature, and CO₂ concentration. Microscopic structuring and intermolecular forces are analyzed together with the dynamic behavior of the studied fluids.



1. INTRODUCTION

A plethora of studies on the properties and application of ionic liquids have been published in the last years, showing the interest, both in the industry and academia on these fluids.^{1–4} The versatility of these fluids, rising from the possibility of developing task-specific fluids through a judicious combination of ions,^{5,6} is among their main advantages. To obtain full development of these advantages, it is required to understand the molecular-level features, which control ionic liquids properties and structuring,⁷ and thus allowing to develop reliable and accurate structure–property relationships.^{8–10} Among the most remarkable technological applications of ionic liquids stands the use of these fluids for CO₂ capture both from flue gases and gas sweetening,^{11–13} and thus the knowledge of molecular factors controlling CO₂ absorption efficiency¹⁴ and the effect of absorbed CO₂ molecules on ionic liquids properties is of pivotal importance.^{15,16}

Despite the importance of liquids, an analysis of the literature show that most of the available studies have been centered up to date in a reduced number of families of ionic liquids.¹⁷ Likewise, recent studies have showed that many families of common ionic liquids show remarkable toxicological and environmental problems.^{18,19} Therefore, new families of ionic liquids have been proposed including ions with better biodegradability and toxicological profiles. Among these new families, those based on the cholinium cation, (2-hydroxyethyl)trimethylammonium, have attracted great attention. Yu et al.²⁰ reported high biodegradability rates for cholinium-based ionic liquids and showed that highly pure compounds could be synthesized through simple and economical procedures. Petkovic et al.²¹ showed the extremely low toxicity of cholinium-based ionic liquids and their adequate

biodegradability, even using the biocompatible term to describe them. In a recent study, Costa et al.²² analyzed the properties of cholinium-based ionic liquids combined with bis-(trifluoromethylsulfonyl)imide anion, using thermophysical and computational tools. The adequate properties of cholinium-based ionic liquids may be improved/maintained using adequate anions. Yu et al.²⁰ synthesized cholinium-based ionic liquids with naphtenic-based anions; among the compounds studied, those including benzoate and salicylate anions showed very good biodegradability properties. Therefore, cholinium benzoate ([BE][CH]) and cholinium salicylate ([SA][CH]) are ionic liquids with adequate toxicology and biodegradability. They may be synthesized through simple procedures at low costs and show remarkable molecular level features (rising both from the structures of anions and cations), which justify their deeper study. Hence, we report in this work a computational study on [BE][CH] and [SA][CH] ionic liquids, Figure 1, pure and after CO₂ absorption, with the objectives of (i) understanding microscopic structuring and intermolecular forces as a function of pressure and temperature, (ii) inferring the relationships between molecular-level and macroscopic thermophysical properties, and (iii) analyzing the absorbed CO₂ effects on cholinium-based ionic liquids and the mechanism of absorption. Yu et al.²⁰ reported density data for [BE][CH] and [SA][CH] from which it may inferred that these ionic liquids have low molar volume in comparison with common ionic liquids such as imidazolium-based ones. It is well-known that large molar volumes favor CO₂ absorption,¹⁵

Received: May 16, 2012

Revised: June 19, 2012

Published: June 27, 2012

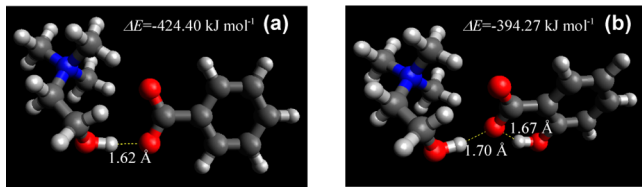


Figure 1. Structures for $[\text{BE}][\text{CH}]$ and $[\text{SA}][\text{CH}]$ ionic pairs obtained from gas phase calculations at B3LYP/6-311++g* theoretical level. ΔE stands for counterpoise corrected interaction energies. Yellow dashed lines show possible hydrogen bonds. Atom color code: (gray) carbon, (blue) nitrogen, (red) oxygen, and (light gray) hydrogen.

and thus we may expect that $[\text{BE}][\text{CH}]$ and $[\text{SA}][\text{CH}]$ show moderate CO_2 solubility. Nevertheless, the objective of this work is not to propose a candidate for industrial CO_2 capture but to understand the molecular level factors controlling absorption mechanism for new families of ionic liquids, especially for environmentally friendly compounds such as those considered in this work.

Computational chemistry tools are powerful approaches for the study of ionic liquids,²³ providing valuable information from the molecular level viewpoint. In this work, we have used a double computational approach for the study of cholinium-based ionic liquids to obtain a wide view of the studied systems:²⁴ (i) quantum chemistry calculations and (ii) classical atomistic molecular dynamics simulations. Quantum chemistry calculations for isolated ions, ion–ion and ion– CO_2 pairs, will lead to information about the charge distribution and transfer, conformational distribution of involved species, and the geometrical and energetic properties of short-range intermolecular interactions.²⁵ We have used density functional theory approach to carry out quantum chemistry calculations considering its accuracy combined with the moderate computational costs for the studied systems.²⁶ Classic atomistic molecular dynamics simulations provide information on the microscopic structuring of the studied fluids, the dynamic properties and the changes of the properties with pressure and temperature. This work is a continuation of our previous studies on environmentally friendly ionic liquids,^{27–29} and it would contribute to the understanding of properties of noncommon biocompatible new ionic liquids.^{30,31}

2. COMPUTATIONAL METHODS

Quantum chemistry calculations were done with the density functional theory (DFT) approach by using the Gaussian 03 package.³² The Becke gradient corrected exchange functional³³ and Lee–Yang–Parr correlation functional³⁴ with three parameters (B3LYP)³⁵ method together with a 6-311++g* basis set was used along this work. Atomic charges were calculated to fit the electrostatic potential³⁶ according to the Merz–Singh–Kollman (MK)³⁷ scheme. For geometry optimization calculations, true minima were confirmed through the absence of imaginary frequencies in the calculated vibrational spectra. Interaction energies for complexes (ion–ion and ion– CO_2), ΔE , were calculated as the differences among the complex and sum of monomers' energies at the same theoretical level with basis set superposition error (BSSE) corrected through the counterpoise procedure.³⁸ Atoms in a molecule (AIM)³⁹ (using the AIM2000 program⁴⁰) and natural bond orbital (NBO)⁴¹ calculations were carried out to get a deeper insight into anion/cation/ CO_2 interactions.

COSMO-RS calculations used to predict CO_2 adsorption in the studied ionic liquids were done with the COSMOthermX⁴² program for structures optimized in Gaussian 03 package at the B3LYP/6-311++g** level, for these optimized structures COSMO files were calculated at the BVP86/TZVP/DGA1 level and used for all the calculations. The model parametrization used for all the physicochemical COSMO calculations was BP_TZVP_C21_0111.

Atomistic classical molecular dynamics simulations were carried out using the MDynaMix v. 5.0 molecular modeling package.⁴³ Molecular dynamics were analyzed to infer structural, energetic, and dynamic properties of the studied fluids. Simulations were performed in the NPT ensemble using the Nose–Hoover method to control the temperature and pressure of the simulation system.⁴⁴ The equations of motion were solved by Tuckerman–Berne double time step algorithm⁴⁵ with long and short time steps of 1 and 0.1 fs, respectively. The Ewald summation method⁴⁶ was implemented for the Coulombic interactions with radius cutoff of 1.5 nm. The simulated systems consist of cubic boxes of pure ionic liquids or ionic liquids with absorbed CO_2 , with the compositions reported in Table S1 (Supporting Information). Initial boxes were generated placing randomly ions and CO_2 molecules in a FCC lattice at low density (~ 0.2 – 0.3 g cm^{-3}), then NPT simulations were performed at the selected pressure and temperature, then several heating and quenching steps (up to 500 K) were done, after that a new NPT simulation was carried out at the selected pressure and temperature (0.1 ns long) to ensure equilibration, which is checked through constant potential energy. After equilibration, 10 ns runs (time step 1 fs) in the NPT ensemble at the studied pressure and temperature were performed for the analysis of systems' properties. Force field parametrization for the studied ionic liquids and CO_2 molecules used along this work is reported in Table S2 (Supporting Information).

3. RESULTS AND DISCUSSION

3.1. Quantum Chemistry Calculations. 3.1.1. Ionic Pairs.

Calculations on the properties and structure of isolated (gas phase) ionic pairs were carried out. The ionic pairs with highest interaction energies, ΔE , are reported in Figure 1. The reported results show hydrogen bonding between $[\text{CH}]^+$ cation and $[\text{BE}]^-$ and $[\text{SA}]^-$, through the cation hydroxyl group and the COO^- group in the corresponding ions. Interaction between $[\text{BE}]^-$ and $[\text{CH}]^+$ is stronger than for $[\text{SA}]^-$ and $[\text{CH}]^+$ pair (7.6% larger ΔE), which is in agreement with the shorter hydrogen bond distance reported in Figure 1. The anion–cation hydrogen bonding is remarkably strong; we have calculated the structure of the $[\text{SA}]^-$ – $[\text{CH}]^+$ ionic pair interacting through the hydrogens in the methyl group, Figure S1 (Supporting Information), the difference between the ΔE values reported in Figure S1 and those reported in Figure 1b ($42.76 \text{ kJ mol}^{-1}$) is a raw measurement of the strength of anion–cation hydrogen bonding. In the case of $[\text{SA}]^-$ – $[\text{CH}]^+$, we should remark that the intramolecular hydrogen bonding in $[\text{SA}]^-$ anion is maintained in comparison with the isolated $[\text{SA}]^-$ anion. Calculations carried out for noninteracting $[\text{SA}]^-$ anion showed that the distance between the hydroxyl oxygen and the oxygen in the COO group is 1.55 Å, which is lower than the values reported in Figures 1b and S1 (Supporting Information). Therefore, the development of $[\text{SA}]^-$ – $[\text{CH}]^+$ interaction weakens the intramolecular hydrogen bonding in $[\text{SA}]^-$ anion, although it is maintained, at least for the gas phase

results reported in this section. In order to quantify the strength of the intramolecular hydrogen bonding in $[\text{SA}]^-$ anion, we have carried out a relaxed torsional scan of the corresponding dihedral angle, Figure 2. The properties of intramolecular

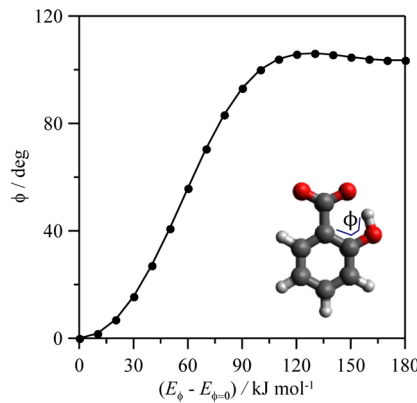


Figure 2. Relaxed dihedral scan for the reported dihedral angle, ϕ , in $[\text{SA}]^-$ anion calculated in gas phase at B3LYP/6-311++g* theoretical level.

hydrogen bonding in $[\text{SA}]^-$ anion are important because it should compete with the development of anion–cation intermolecular hydrogen bonding as reported in Figure 1b. The results reported in Figure 2 show a strong intramolecular hydrogen bonding for isolated $[\text{SAL}]^-$ anion with a large torsional barrier. This large barrier would hinder the out-of-plane movement of hydroxyl group in $[\text{SA}]^-$ anion, and thus, hydroxyl group would act as and hydrogen bond acceptor but not as donor. We have analyzed the possibility of developing $[\text{SA}]^-$ – $[\text{CH}]^+$ hydrogen bonding through the hydroxyl group in the cation, Figure S2 (Supporting Information), the reported results show that the interaction through this position is remarkably weaker than the interaction through the COO group in $[\text{SA}]^-$. In fact, the interaction through the $[\text{SA}]^-$ hydroxyl group evolves toward the minimum energy structure reported in Figure S1 (Supporting Information). The possible

reason for the preferential interaction between $[\text{SA}]^-$ and $[\text{CH}]^+$ ions through the COO group may rise from the stronger Coulombic interactions developed through this position in comparison with those for the structure reported in Figure S2 (Supporting Information).

Another important factor for the analysis of the studied ionic pairs is the charge transfer upon ionic pair formation. MK charges were calculated for those ionic pairs reported in Figure 1 and are included in Figure S3 (Supporting Information). The MK values show that the charge of the involved ions is ± 0.824 for the $[\text{BE}]^-$ – $[\text{CH}]^+$ pair and ± 0.802 for the $[\text{SAL}]^-$ – $[\text{CH}]^+$ pair and thus showing a remarkable charge transfer between the corresponding ions. Likewise, the calculated bond length for the hydroxyl group in $[\text{CH}]^+$ cation is 0.965, 1.006, and 0.991 Å, for the isolated cation ($\nu(\text{OH}) = 3791 \text{ cm}^{-1}$, calculated unscaled wavenumber), for the cation in $[\text{BE}]^-$ – $[\text{CH}]^+$ pair ($\nu(\text{OH}) = 2987 \text{ cm}^{-1}$), and for the cation in the $[\text{SA}]^-$ – $[\text{CH}]^+$ pair ($\nu(\text{OH}) = 3229 \text{ cm}^{-1}$), respectively. Therefore, these values confirm the development of strong hydrogen bonding upon ionic pair formation, being remarkably stronger for the $[\text{BE}]^-$ containing pair.

We should remark an apparent discrepancy between the MK charges obtained for ionic pairs reported in the previous section ($\approx \pm 0.8$ total charge for anion and cation) and the charges used for molecular dynamics simulations (± 1 total charge for anion and cation). The reasons for this approach were the following: (i) one of our objectives is developing transferable forcefields, and thus, ± 1 ion charges forcefields are more suitable for this purpose; (ii) DFT results show information on short-range interactions, which is reflected by the reported charge transfer, and the effect of long-range interaction on charge transfer could not be analyzed because the size limitation for quantum chemistry studies; (iii) the use of ± 0.8 ion charges leaded to a very polarized molecular model, which physical properties were different to those experimental ones.

AIM and NBO analysis provide more detailed information about the way in which the studied ions interact. We report in Figure 3 the results of AIM analysis for the lowest energy structures of the studied ionic pairs. AIM analysis of $[\text{BE}]^-$ –

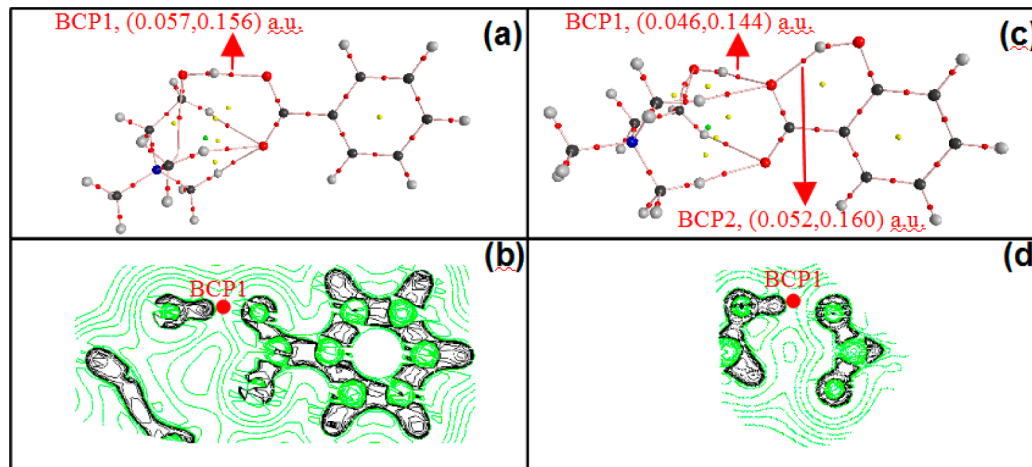


Figure 3. (a,c) AIM analysis of the lowest energy ionic pairs showing bond critical points (BCP, red circles), ring critical points (yellow circles), and cage critical points (green circles), including data for electron density and laplacian of electron density at relevant BCPS (in this order). (b,d) Contour plot for the Laplacian of electron density, $\nabla^2\rho_{\text{BCP}}$; green curves represent positive isosurface values of $\nabla^2\rho_{\text{BCP}}$ and black curves represent negative isosurface values of $\nabla^2\rho_{\text{BCP}}$. In panels b and c, we report only bond paths (pink lines) but not ring and cage paths for the sake of visibility. In panel d, hydroxyl group in $[\text{CH}]^+$ and aromatic ring in $[\text{SA}]^-$ are not coplanar, see panel c, and thus contour plot was showed only for the intermolecular hydrogen bonding.

$[\text{CH}]^+$ pair, Figure 3a,b, shows the appearance of a bond critical point (BCP) in the middle of the path between the cation hydroxyl and anion CO group. The considered criteria to define a hydrogen bonding according to AIM approach stands that the electron density at BCP, ρ_{BCP} , and the Laplacian of that electron density, $\nabla^2\rho_{\text{BCP}}$, must be in the 0.002–0.035 and 0.024–0.139 ranges, respectively; the values reported in Figure 3a for ρ_{BCP} and $\nabla^2\rho_{\text{BCP}}$ show a very strong anion–cation hydrogen bonding. The behavior of $\nabla^2\rho_{\text{BCP}}$ reported in Figure 3b shows remarkable charge depletion ($\nabla^2\rho_{\text{BCP}} > 0$) between the cation hydroxyl group and the anion CO group corresponding to strong hydrogen bonding. For the $[\text{SA}]^- - [\text{CH}]^+$ pair analogous results are obtained, Figure 3c,d, but the intermolecular BCP (BCP1) is weaker than for $[\text{BE}]^- - [\text{CH}]^+$, as the lower ρ_{BCP} and $\nabla^2\rho_{\text{BCP}}$ show, which is agreement with the weaker energies reported in Figure 1. Likewise, intramolecular hydrogen bonding in $[\text{SA}]^-$ is remarkably strong (BCP2).

The NBO analysis is carried out according to the second order perturbation theory analysis of Fock matrix in NBO basis, considering for the analysis of interactions (i) the second-order perturbation energy, $E(2)$, (ii) the energy difference among the donor and the acceptor, ΔE , and (iii) Fock matrix element between the donor and acceptor, F_{ij} , reflecting the symmetry between donor and acceptor orbitals. Stronger hydrogen bonding is obtained for larger $E(2)$ values, which may rise from low ΔE and/or large F_{ij} values (better donor–acceptor symmetry for larger F_{ij} values), both factors contributing to improve the donor–acceptor charge transfer. Results for ion pairs are reported in Table 1, intermolecular hydrogen bonding rises from the hyperconjugation-induced charge transfer between the oxygen electron lonely pairs in anion COO groups (donor) and the antibonding orbitals for the hydroxyl group in $[\text{CH}]^+$ (acceptor), $n_{\text{O}} \rightarrow \sigma^*_{\text{O}-\text{H}}$. $E(2)$ values for $[\text{BE}]^- - [\text{CH}]^+$ pair are remarkably larger than for $[\text{SA}]^- - [\text{CH}]^+$ pair. In the case of $[\text{BE}]^- - [\text{CH}]^+$ pair, we should remark the very large interaction rising from the second lone pair in oxygen for $[\text{BE}]^-$, which may be justified considering the low donor–acceptor energy difference and the good symmetry between both orbitals. For $[\text{SA}]^- - [\text{CH}]^+$, although strong intermolecular hydrogen bonding may be inferred, the interactions are clearly less optimal than for the $[\text{BE}]^- - [\text{CH}]^+$ case, which may be justified considering the poorest donor–acceptor symmetry for the second oxygen donor pair. $[\text{SA}]^- - [\text{CH}]^+$ intermolecular interaction should be affected by the development of intramolecular hydrogen bonding in $[\text{SA}]^-$ anion, NBO results reported in Table 1 confirm the strong intramolecular hydrogen bonding, specially through the second oxygen donor pair. Likewise, the donor–acceptor symmetry in $[\text{SA}]^- - [\text{CH}]^+$ for the intramolecular hydrogen bonding through the second donor pair is better than for the intermolecular anion–cation second donor pair, as the F_{ij} values show. Therefore, the weaker character of intermolecular hydrogen bonding in $[\text{SA}]^- - [\text{CH}]^+$ rises from the worse donor–acceptor symmetry, which is produced by the simultaneous development of intramolecular and intermolecular hydrogen bonding for $[\text{SA}]^-$ anion.

3.1.2. Ions + CO_2 Pairs. Quantum chemistry methods used for the study of ion–ion pairs were also applied for the analysis of the properties of ion– CO_2 pairs to infer the affinity of each involved ion for the CO_2 molecules. We report in Figure 4 the optimized structures for the corresponding ion– CO_2 pairs. The interaction of both anions leads to a T-shaped structure, with

Table 1. NBO Analysis of Ion–Ion and Ion– CO_2 Pairs Computed in Gas Phase at B3LYP/6-311++g* Theoretical Level^a

pair	donor	donor pair	acceptor	$E(2)/\text{kJ mol}^{-1}$	$\Delta E/\text{au}$	F_{ij}/au
^b $[\text{BE}]^- - [\text{CH}]^+$	O in $[\text{BE}]^-$	LP 1	OH in $[\text{CH}]^+$	27.87	1.04	0.075
		LP 2	OH in $[\text{CH}]^+$	128.24	0.70	0.133
^b $[\text{SA}]^- - [\text{CH}]^+$	O in $[\text{SA}]^-$	LP 1	OH in $[\text{CH}]^+$	43.72	1.13	0.097
		LP 2	OH in $[\text{CH}]^+$	40.58	0.69	0.074
	O in $[\text{SA}]^-$	LP 1	OH in $[\text{SA}]^-$	34.64	1.12	0.086
		LP 2	OH in $[\text{SA}]^-$	71.55	0.68	0.098
^c $[\text{BE}]^- - [\text{CO}_2]$	^d O in $[\text{BE}]^-$	LP 2	C in $[\text{CO}_2]$, LP* ₁	7.36	0.08	0.013
		LP 2	C in $[\text{CO}_2]$, LP* ₂	23.81	0.08	0.023
^c $[\text{SA}]^- - [\text{CO}_2]$	^e O(1) in $[\text{SA}]^-$	LP 2	C–O in CO_2	6.78	0.23	0.018
	^e O(2) in $[\text{SA}]^-$	LP 2	C–O in CO_2	3.56	0.30	0.015
^c $[\text{CH}]^+ - [\text{CO}_2]$	O in CO_2	LP 1	OH in $[\text{CH}]^+$	9.71	1.21	0.048
	O in CO_2	LP 2	OH in $[\text{CH}]^+$	2.85	0.75	0.022

^aSecond-order perturbation energy, $E(2)$, energy difference among the donor and the acceptor, ΔE , and Fock matrix element between the donor and the acceptor, F_{ij} . All values reported for the optimized structures of the corresponding pairs. ^bValues for optimized structures in Figure 1. ^cValues for optimized structures in Figure 4. ^dThis interaction appears twice: one for each oxygen in $[\text{BE}]^-$ COO group. ^eO(1) and O(2) stand for oxygen atom not involved and involved, respectively, in intramolecular hydrogen bonding (with $[\text{SA}]^-$ hydroxyl group) for $[\text{SA}]^-$.

bending of the O–C–O angle in CO_2 . $[\text{BE}]^-$ interacts more effectively with CO_2 molecule than $[\text{SA}]^-$, which leads to larger interaction energies, shorter intermolecular distances, and stronger CO_2 bending. In the case of $[\text{SA}]^- - \text{CO}_2$ pair, the intermolecular interaction do not change remarkably the intramolecular hydrogen bonding in $[\text{SA}]^-$ anion, for the isolated $[\text{SA}]^-$ anion the intramolecular hydrogen bond is characterized by a 1.55 Å distance, which is only slightly increased by the interaction with CO_2 molecule, Figure 4b. Moreover, the vibrational frequency for the hydroxyl group in $[\text{SA}]^-$ anion is 3757 cm⁻¹ for $[\text{SA}]^- - \text{CO}_2$, which is only slightly lower than the 3791 cm⁻¹ calculated for the isolated $[\text{SA}]^-$ anion. Likewise, $[\text{CH}]^+ - \text{CO}_2$ interaction leads to the development of intermolecular hydrogen bonding, although cation– CO_2 interaction energy is remarkably lower than anion– CO_2 energy, for both studied anions. Therefore, considering the quantum chemistry results it may be expected larger CO_2 absorption capacity for the $[\text{BE}][\text{CH}]$ ionic liquid, if only intermolecular affinity were considered.

AIM analysis of ions– CO_2 pairs provide information on the topological reasons for the reported different affinities, Figure 5. For $[\text{BE}]^- - [\text{CO}_2]$ pair, two identical BCP are inferred, Figure 5a, with $\nabla^2\rho_{\text{BCP}} > 0$ along the bond path joining both molecules, Figure 5b. In the case of $[\text{SAL}]^- - \text{CO}_2$ pair, two BCP are also obtained, BCP1 and BCP 2 in Figure 5c, but the properties of both BCPs are slightly different, and in both cases slower ρ_{BCP} and $\nabla^2\rho_{\text{BCP}}$ than for $[\text{BE}]^- - [\text{CO}_2]$ are obtained,

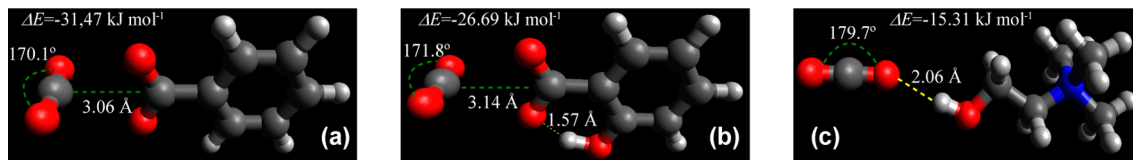


Figure 4. Structures for (a) $[\text{BE}]^-$ - $[\text{CO}_2]$, (b) $[\text{SA}]^-$ - CO_2 and (c) $[\text{CH}]^+$ - CO_2 pairs obtained from gas phase calculations at B3LYP/6-311++g* theoretical level. ΔE stands for counterpoise corrected interaction energies. Yellow dashed lines show possible hydrogen bonds, green dashed lines show ion- CO_2 distance O-C-O angle in CO_2 . Atom color code: (gray) carbon, (blue) nitrogen, (red) oxygen, and (light gray) hydrogen.

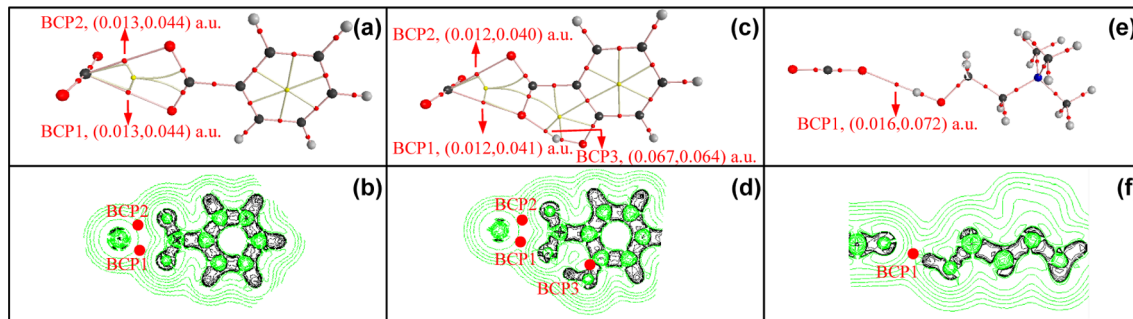


Figure 5. (a,c,e) AIM analysis of the lowest energy ionic pairs showing bond critical points (BCP, red circles), ring critical points (yellow circles), and cage critical points (green circles), including data for electron density and laplacian of electron density at relevant BCPs (in this order). (b,d,f) Contour plot for the Laplacian of electron density, $\nabla^2\rho_{\text{BCP}}$; green curves represent positive isosurface values of $\nabla^2\rho_{\text{BCP}}$ and black curves represent negative isosurface values of $\nabla^2\rho_{\text{BCP}}$.

which would justify the weaker ΔE values reported in Figure 4 for $[\text{SAL}]^-$ - CO_2 pair. The intramolecular hydrogen bonding in $[\text{SAL}]^-$ is also characterized by a BCP, BCP3 in Figure 5c, and the values of ρ_{BCP} and $\nabla^2\rho_{\text{BCP}}$ show the strength of this interaction maintained upon interaction with CO_2 molecules. The $[\text{CH}]^+$ - CO_2 pair is characterized by an intermolecular hydrogen bonding, BCP1 in Figure 5e, the ρ_{BCP} and $\nabla^2\rho_{\text{BCP}}$ values for that interaction are in the middle of the aforementioned range to define hydrogen bonding according to AIM criteria, and thus a moderate hydrogen bonding may be inferred, which is in agreement with the charge depletion showed by the $\nabla^2\rho_{\text{BCP}}$ behavior reported in Figure 5f.

Results of NBO analysis are included in Table 1. The stronger interactions for the $[\text{BE}]^-$ - $[\text{CO}_2]$ pair in comparison with the $[\text{SAL}]^-$ - CO_2 pair are explained considering the remarkably larger $E(2)$ obtained, which are justified considering the lower energy differences and the better symmetry for donor-acceptor in the $[\text{BE}]^-$ case. In the case of $[\text{CH}]^+$ - CO_2 pairs, the intermolecular hydrogen bonding is characterized by the moderate symmetry between the donor and the acceptor coupled with remarkable energy differences, both factors leading to the moderate ΔE values reported in Figure 4 in comparison with those for anion- CO_2 pairs.

3.2. Molecular Dynamics Simulations. **3.2.1. Methods and Forcefield Validation.** One of the most remarkable aspects for the development of predictive conclusions from molecular dynamics simulations is the need of long enough simulations to avoid wrong conclusions obtained from simulations in which involved ions are trapped in local cages, and thus, a true picture of the fluid's behavior is not inferred. This is especially important for highly viscous ionic liquids as the ones studied in this work²⁰ for which low diffusion rates are obtained and thus longer simulations are required. Nevertheless, the large number of systems and conditions studied in this work hinders to carry out very long simulations because of time constraints, and thus, a compromise solution was developed between simulation

lengths and accuracy. We have analyzed the behavior of the potential energy for the studied systems as a function of simulation time, and the reported results show that the procedure proposed in this work lead to representative pictures of the studied systems, as the almost constancy of the systems' potential energy shows, Figure S4 (Supporting Information).

The reliability of molecular dynamics simulations also stands on the ability of the used forcefield parametrization to reproduce accurately relevant thermophysical properties of the studied systems. Maginn²³ considered the use vaporization enthalpies as the most suitable property for validation purposes; likewise, Maginn considered the problems of using density predictions as a validation tool because of the mean field character of this property. Nevertheless, vaporization enthalpy data are absent in the literature for new families of ionic liquids as the one considered in this work, which hinder any comparison. Moreover, experimental vaporization enthalpies available in the literature for common ionic liquids families were measured using different experimental approaches, which lead to remarkable differences between the reported data, and thus hindering their use for forcefield validation purposes. These absence of experimental data is particularly remarkable for $[\text{BE}][\text{CH}]$ and $[\text{SA}][\text{CH}]$. Therefore, we have used available density in a first validation step for $[\text{BE}][\text{CH}]$ and $[\text{SA}][\text{CH}]$, Figure 6. An excellent agreement between experimental and predicted data is obtained, especially for $[\text{SA}][\text{CH}]$. Deviations with experimental data are 0.93 and 0.04% for $[\text{BE}][\text{CH}]$ and $[\text{SA}][\text{CH}]$, respectively. Therefore, it may be concluded the adequate ability of the proposed forcefield parametrization for the accurate prediction of volumetric properties.

Yu et al.²⁰ reported experimental viscosity data at 313.15 K for the studied ionic liquids, and thus we have predicted dynamic viscosity using molecular simulations for comparison purposes. Self-diffusion coefficients, D , were obtained from molecular dynamics simulation trajectories using Einstein's

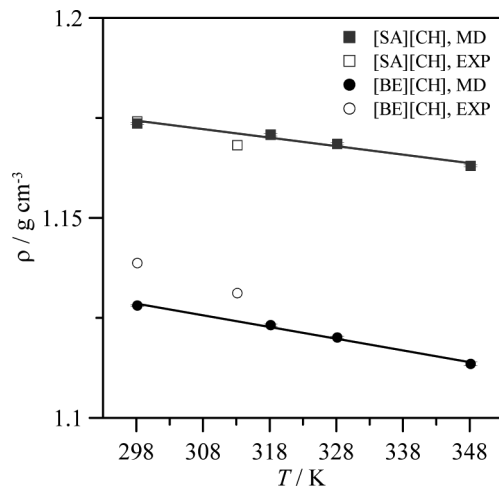


Figure 6. Comparison of density data predicted from molecular dynamics simulations and experimental data from Yu et al.²⁰ Continuous lines are linear fits of predicted density data for guiding purposes.

relation, and dynamic viscosity, η , using Green–Kubo equation, Table 2. Calculated D values are reasonable considering the

Table 2. Self-Diffusion Coefficient, D , and Dynamic Viscosity, η , Obtained from Molecular Dynamics Simulations in Comparison with Available Experimental Data^a

ionic liquid	simulated		experimental ^b	
	$10^{11} \times D_{\text{ANION}}/\text{m}^2 \text{ s}^{-1}$	$10^{11} \times D_{\text{CATION}}/\text{m}^2 \text{ s}^{-1}$	$\eta/\text{mPa s}$	$\eta/\text{mPa s}$
[BE] [CH]	0.19 ± 0.02	0.16 ± 0.02	1233 ± 125	1096.73
[SA] [CH]	0.15 ± 0.02	0.13 ± 0.01	1540 ± 160	1192.31

^aSimulated D values were calculated from mean square displacements by Einstein's relationship, and simulated η values were calculated using the Green–Kubo equation. All values at 313.15 K, 0.1 MPa. ^bData from Yu et al.²⁰

large viscosity of the studied ionic liquids. Calculated η values are in good agreement with experimental results, although predicted η is larger than experimental data (13 and 29% for [BE][CH] and [SA][CH], respectively), predictive ability of

the proposed forcefield parametrization is in the range of the available literature studies for other families of ionic liquids considering the well-known difficulties for capturing dynamic behavior of viscous ionic liquids because of their sluggish character.^{47–49}

3.2.2. Pure Ionic Liquids. The structuring of pure ionic liquids were initially analyzed using radial distribution functions, RDFs. Center of mass, c.o.m., RDFs are reported in Figure 7 for the corresponding interacting pairs. The most remarkable feature inferred from results reported in Figure 7 is the scarce differences between RDFs for [BE][CH] and [SA][CH] ionic liquids. Anion–cation interaction, Figure 7a, is characterized by a strong peak at 5.35 Å for [BE][CH], which is shifted to 5.65 Å for [SA][CH]. Anion–cation RDFs show a first minimum at ~7.5 Å integrating to ~6 ions. Anion–anion interactions, Figure 7b, are not characterized by remarkable interactions, and the hydroxyl group in [SA]⁻ does not change this feature in comparison with [BE]⁻. On the contrary, cation–cation interactions are characterized by a complex behavior, leading to three well-defined peaks, Figure 7c.

The interaction between the involved ions can be analyzed more in detail using specific site, site RDFs, Figure 8. The analysis of RDFs for the H4 ([CH]⁺)–O2 ([BE]⁻ or [SA]⁻) pair, Figure 8a, shows a strong anion–cation hydrogen bonding with RDFs peaking at 1.95 Å and a first minimum at ~3.15 Å integrating to ~0.6 ions. In the case of [SA][CH] ionic liquid, the presence of hydroxyl group in [SA]⁻ could lead to the development of interionic hydrogen bonding through this site; nevertheless, the results reported in Figure 8a show that anion–cation hydrogen bonding through the anion hydroxyl bonding is clearly less important than through the COO group. Cation–cation interaction is analyzed through the H4 ([CH]⁺)–O1 ([CH]⁺) pair, Figure 8b, which discards the development of hydrogen bonding. For the case of anion–anion interaction in [SA][CH], we report in Figure 8c RDFs for the possible interaction sites, discarding the development of hydrogen bonding.

Although RDFs provide with valuable information about ion–ion interactions, they do not lead to the relevant information about the spatial arrangement of involved molecules, which can be inferred from spatial distribution functions, SDFs. Anion–cation interactions are characterized by the distribution of hydrogen atoms in [CH]⁺ hydroxyl group around the corresponding anions, Figure 9. Results reported in Figure 9 show the arrangement of [CH]⁺ cation hydroxyl

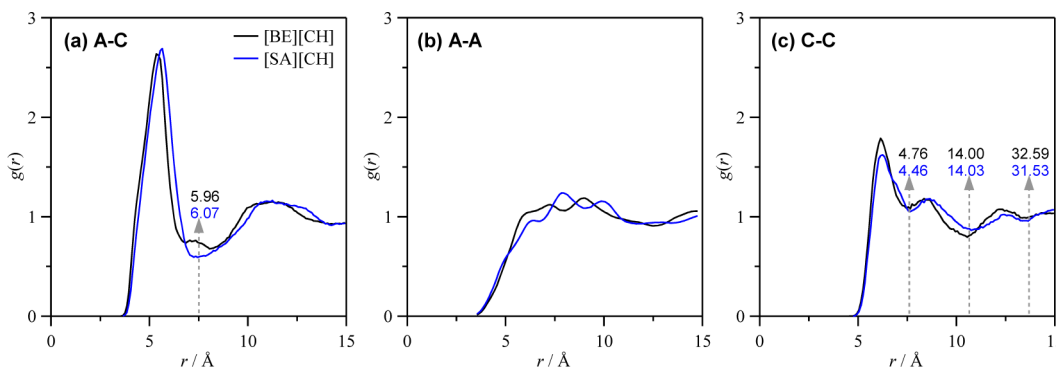


Figure 7. Center of mass radial distribution functions, $g(r)$, for pure [BE][CH] and [SA][CH], obtained from molecular dynamic simulations at 328 K, 0.1 MPa. Dashed arrows show the $g(r)$ minima values, and values inside panels a and c show the values of the running integrals for each corresponding minima. A and C stand for anion and cation, respectively.

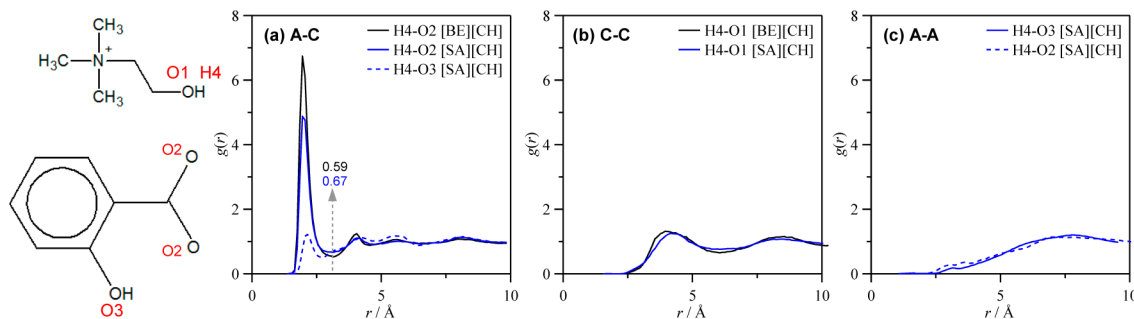


Figure 8. Site–site radial distribution functions, $g(r)$, for pure $[\text{BE}][\text{CH}]$ and $[\text{SA}][\text{CH}]$, obtained from molecular dynamic simulations at 328 K, 0.1 MPa. Dashed arrow in show the $g(r)$ minima values, and values inside panel a show the values of the running integrals for each corresponding minima.

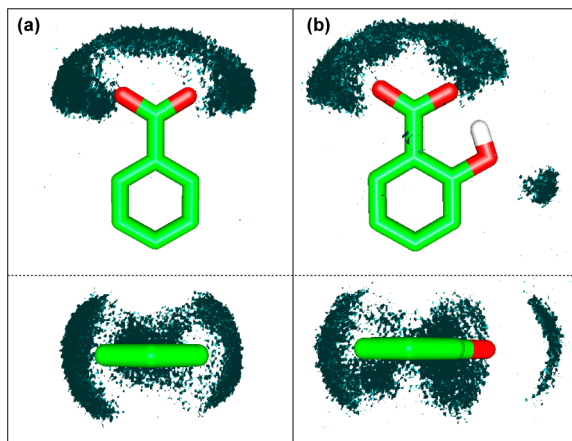


Figure 9. Spatial distribution functions of hydroxyl hydrogens in $[\text{CH}]^+$ cations (H4 atoms, Figure 8) around (a) $[\text{BE}]^-$ and (b) $[\text{SA}]^-$ anions for (a) $[\text{BE}][\text{CH}]$ and (b) $[\text{SA}][\text{CH}]$ ionic liquids at 328 K, 0.1 MPa obtained from molecular dynamic simulations. Blue surfaces show 15 times bulk density.

groups around the COO group both for $[\text{BE}]^-$ and $[\text{SA}]^-$ anions with a remarkable density cap extended along the COO anion group. In the case of $[\text{SA}][\text{CH}]$, weaker interactions are also developed through the $[\text{SA}]^-$ hydroxyl group, although clearly less important than through the COO site. The average structure for $[\text{SA}]^-$ anion reported in Figure 9b, shows that intramolecular hydrogen bonding is maintained in spite of the presence of $[\text{CH}]^+$ cation, although the presence of anion could lead to an out-of-plane rotation of the hydroxyl group in $[\text{SA}]^-$ anion for developing stronger anion–cation hydrogen bonding, the calculated torsional distribution reported in Figure 10 shows that this effect is not produced for $[\text{SA}][\text{CH}]$ system. This effect is in agreement with the quantum chemistry results reported in previous sections, showing the preferential anion–cation interaction through the COO anion site. The average number of anion–cation hydrogen bonds were calculated from molecular simulation results with donor–acceptor distance equal to 3.15 Å (the first minimum in the H4, cation, O2, anion, RDFs reported in Figure 8a) and 30° as the limit value for the donor–acceptor angle. On average, 0.56 ± 0.04 and 0.46 ± 0.04 hydrogen bonds (per ion) through the anion COO site were obtained for $[\text{BE}][\text{CH}]$ and $[\text{SA}][\text{CH}]$ at 318 K, 0.1 MPa, respectively. For $[\text{SA}][\text{CH}]$, 0.07 ± 0.02 hydrogen bonds (per ion) were obtained through the $[\text{SA}]^-$ hydroxyl site. Therefore, the introduction of hydroxyl group in anion ring decreases the number of anion–cation hydrogen bonds

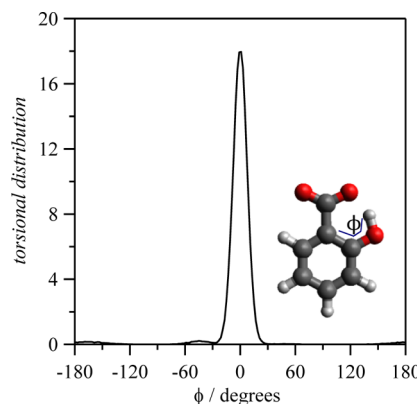


Figure 10. Torsional distribution of dihedral angle involving hydroxyl group in $[\text{SA}]^-$ anion for $[\text{SA}][\text{CH}]$ ionic liquid at 328 K, 0.1 MPa obtained from molecular dynamic simulations.

through the COO anion position, but it is compensated by hydrogen bonding through the hydroxyl position, leading to the number of total anion–cation hydrogen bonds being almost the same for $[\text{BE}][\text{CH}]$ and $[\text{SA}][\text{CH}]$.

A remarkable property for the characterization of ionic liquids is the void volume available, which is especially important for gas solubility purposes. The distribution of cavity sizes for pure ionic liquids were calculated according to the method proposed by Margulis⁵⁰ measuring the smallest distance of random points to all atoms in the fluids, Figure 11. The cavity size distribution is almost equivalent for

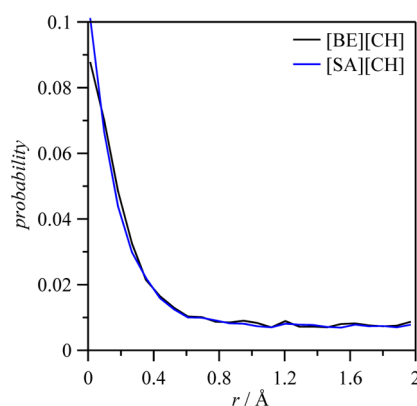


Figure 11. Distribution of cavity sizes in pure $[\text{BE}][\text{CH}]$ and $[\text{SA}][\text{CH}]$ at 328 K, 0.1 MPa obtained from molecular dynamic simulations.

Table 3. Intermolecular (Interionic) Interaction Energies, Split in Lennard-Jones, LJ, and Electrostatic, ELE, Contributions, for [BE][CH] and [SA][CH] Obtained from Molecular Dynamics Simulations As a Function of Temperature and 0.1 MPa^a

T/K	A–A		A–C		C–C	
	LJ	ELE	LJ	ELE	LJ	ELE
[BE][CH]						
298	-15.62 ± 0.01	1094.09 ± 0.48	-36.19 ± 0.02	-2671.04 ± 0.63	-14.87 ± 0.01	1114.46 ± 0.32
318	-15.29 ± 0.01	1091.18 ± 0.45	-36.34 ± 0.02	-2664.81 ± 0.56	-14.7 ± 0.01	1113.85 ± 0.33
328	-15.65 ± 0.01	1087.88 ± 0.54	-35.40 ± 0.02	-2652.13 ± 0.71	-14.86 ± 0.01	1110.34 ± 0.34
348	-15.12 ± 0.01	1074.02 ± 0.40	-35.69 ± 0.02	-2632.94 ± 0.91	-14.63 ± 0.01	1095.11 ± 0.43
[SA][CH]						
298	-16.25 ± 0.02	1073.54 ± 0.60	-40.48 ± 0.02	-2594.66 ± 0.61	-13.83 ± 0.01	1066.03 ± 0.28
318	-15.84 ± 0.03	1057.97 ± 0.67	-40.85 ± 0.02	-2587.71 ± 0.58	-13.79 ± 0.01	1070.13 ± 0.36
328	-16.17 ± 0.01	1057.86 ± 0.64	-40.63 ± 0.03	-2590.45 ± 0.72	-13.77 ± 0.01	1067.22 ± 0.42
348	-15.93 ± 0.02	1056.30 ± 0.70	-40.67 ± 0.03	-2565.73 ± 0.73	-13.32 ± 0.01	1060.54 ± 0.41

^aAll values in kJ mol⁻¹. A stands for anion and C stands for cation.

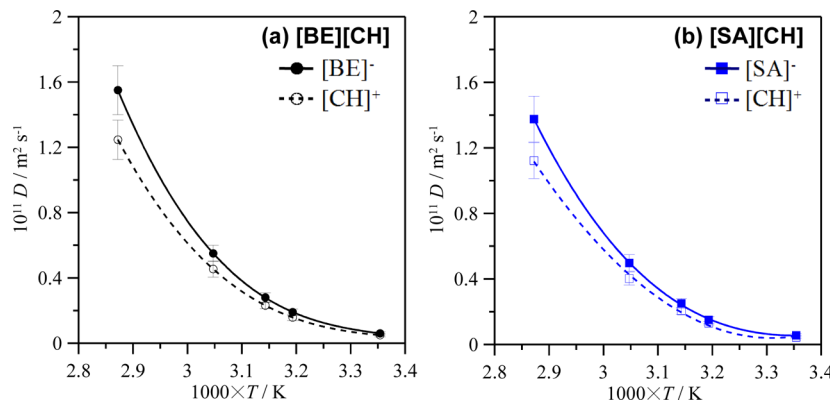


Figure 12. Self-diffusion coefficients, D , for anion and cation in pure [BE][CH] and [SA][CH] as a function of temperature at 0.1 MPa, obtained from molecular dynamic simulations. All values calculated using Einstein's relationship from mean square displacements. Lines show polynomial fits for guiding purposes.

[BE][CH] and [SA][CH]. The free volume was calculated as the difference between the molar volume and the molecular volume calculate from Connolly method, leading to 60.43 (0.27 cm³ g⁻¹) and 61.02 cm³ mol⁻¹ (0.25 cm³ g⁻¹) at 328 K, 0.1 MPa for [BE][CH] and [SA][CH], respectively. In a recent work, Shannon et al.⁵¹ proposed a new alternative method for calculating free volume using COSMOtherm approach, therefore to compare results for [BE][CH] and [SA][CH] with those reported for imidazolium-based compounds we have applied the same method than Shannon et al.⁵¹ Therefore, the obtained free volume using the COSMOtherm approach were 26.24 and 26.50 cm³ mol⁻¹ for [BE][CH] and [SA][CH], respectively. These COSMOtherm free volume values are in the range of middle-sized imidazolium-based cations (close to those containing butyl chains),⁵¹ and thus, although cavity sizes reporter in Figure 11 for [BE][CH] and [SA][CH] are small, they could rearrange leading to remarkable accessible volume for applications such as gas solubility.

Intermolecular interaction energies were calculated from molecular dynamics results, Table 3. The calculated interaction energies are very similar for [BE][CH] and [SA][CH] for all the studied ion pairs. For anion–cation interaction energies LJ contributions are 12–13% larger in absolute value for [SA][CH] than for [BE][CH], which may be justified considering the presence of the anion hydroxyl group. Nevertheless, anion–cation ELE term is 2.5–3.0% larger for [BE][CH] than for [SA][CH]. Therefore, differences between the studied ionic liquids from the viewpoint of interaction

energy are almost negligible, at 328 K, 0.1 MPa, the difference between the total intermolecular interaction energy for both ionic liquids is just a 3%. The percentage of LJ contribution for the total intermolecular interaction energy is 12.6 and 13.3% for [BE][CH] and [SA][CH], respectively, in the studied temperature range. Therefore, a slightly larger LJ contribution is inferred for [SA][CH], raising from the anion–cation interaction, nevertheless the difference with [BE][CH] is low to have considerable structural effects. The effect of temperature on intermolecular interaction energies is almost negligible in the 298–348 K range studied. In a previous work, we analyzed the properties of the [LACTATE][CH] ionic liquid,²⁹ the comparison of these results with those reported in this work showed that the ordering in absolute value of anion–cation LJ energies is lactate < [BE]⁻ < [SA]⁻, whereas for ELE term the reverse trend is inferred. The bulkiest character of [BE]⁻ and [SA]⁻ anions in comparison with lactate one, together with the steric hindrance rising from the shape of aromatic ring in these anions, seems to hinder the anion–cation electrostatic interactions when compared with lactate anion. On the contrary, anion–anion interaction is more effective for [BE]⁻ and [SA]⁻ anions than for lactate when paired with [CH]⁺, which could be justified considering the charge delocalization through the aromatic ring in the corresponding ions.

The behavior of dynamic properties of the studied ionic liquids was done using the self-diffusion coefficient, D , obtained using the Einstein's relationship

$$D = \frac{1}{6} \lim_{t \rightarrow \infty} \frac{d}{dt} \langle \Delta r(t)^2 \rangle \quad (1)$$

where the quantity in brackets is the mean square displacement (msd). [BE][CH] and [SA][CH] are very viscous fluids,²⁰ and thus, capturing their dynamic behavior would require long simulation times for reaching fully diffusive regimes. In previous works,²⁰ we showed the usefulness of the so-called β parameter, eq 2, for analyzing if fully diffusive regime ($\beta = 1$) was reached in the used simulation time.^{12,52,53}

$$\beta(t) = \frac{d \log_{10} \langle \Delta r(t)^2 \rangle}{d \log_{10} t} \quad (2)$$

Using this approach, β values in the 0.80–0.90 range were obtained for both ionic liquids for simulations in the 298–348 K range. D values are reported in Figure 12, we concluded that $D_{\text{ANION}} > D_{\text{CATION}}$ (~22% larger for both ionic liquids) for both ionic liquids, which can be justified considering the more remarkable cation–cation structuring reported in Figure 7c in comparison with those for anion–anion, Figure 7b. Likewise, D for [CH]⁺ cation is larger in [BE][CH] than in [SA][CH], which may be justified considering the [CH]⁺ hydrogen bonding both with hydroxyl and COO group in [SA]⁻. The comparison with previous results for [LACTATE][CH]²⁹ shows D ordering as lactate < [BE]⁻ < [SA]⁻, which is in agreement with interaction energies reported in previous paragraph and with experimental dynamic viscosities (viscosity for [LACTATE][CH] is around the half of [BE][CH] and [SA][CH]). Molecular dynamics results allows the calculation of dynamic viscosity, Figure 13, leading to on average 18%

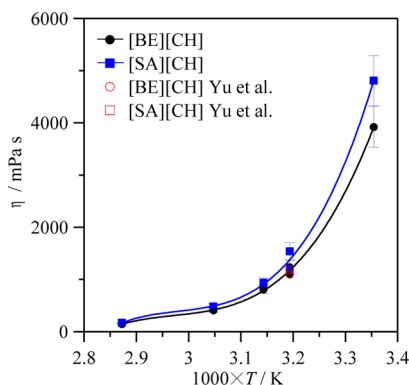


Figure 13. Dynamic viscosity, η , for pure [BE][CH] and [SA][CH] as a function of temperature at 0.1 MPa, obtained from molecular dynamic simulations using the Green–Kubo method. Literature values obtained from Yu et al.²⁰ Lines show polynomial fits for guiding purposes.

larger viscosity values for [SA][CH] than for [BE][CH], and to values remarkably larger than for [LACTATE][CH]. The comparison of results for [LACTATE][CH] with [BE][CH]/[SA][CH] shows that the presence of anions with aromatic rings increases remarkably the fluid viscosity, which may be justified only in part through the changes in intermolecular energies, as reported in previous sections, but also steric effects rising from molecular shapes should play a remarkable role. Yu et al.²⁰ considered stacking effects and interactions between aromatic rings as the origin of the large viscosities in [BE][CH] and [SA][CH]. Results reported in Figure 7b discard the

existence of remarkable anion–anion interactions for both ionic liquids

3.2.3. Ionic Liquids + Adsorbed CO₂ Molecules. The properties and structure of the studied ionic liquids mixed with CO₂ were studied as a function of CO₂ mole fraction. To prepare the simulated systems, CO₂ absorption ability of both ionic liquids is required, and thus adsorption isotherms at 318 K were predicted using the COSMOthermX⁴² approach, Figure 14. COSMOthermX have been used in the literature to predict

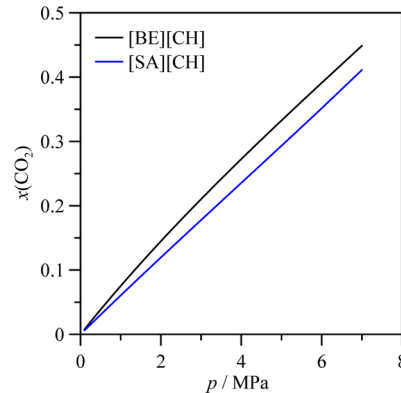


Figure 14. CO₂ Absorption isotherms for [BE][CH] and [SA][CH] ionic liquids at 328 K, calculated with COSMOthermX.⁴²

CO₂ solubility, mainly for screening purposes before going to costly experimental measurements.^{54,55} Ab-Manam et al.⁵⁶ showed that COSMOthermX is able to predict at least in qualitative way gas solubilities in ionic liquids, leading to reliable predictions of the solubility order of magnitude. Therefore, COSMOthermX predictions reported in Figure 14 could be considered a first approach of CO₂ solubility data, and thus, the calculated isotherms were used to define the conditions (x_{CO_2} and pressure) used for molecular dynamics simulations, Table S2 (Supporting Information). COSMOthermX predicts slightly lower CO₂ solubility in [BE][CH] than in [SA][CH], although these results should be taken with caution considering the quantitative predictive ability of COSMOthermX approach.⁵⁶

Literature studies have showed the importance of volumetric effects on the analysis of CO₂ solubility in ionic liquids. Huang et al.⁵⁷ studied the CO₂ solubility in ionic liquids considering the rearrangement of available empty cavities. Likewise, it has been reported as the moderate volume expansion,⁵⁸ low partial molar volume, in ionic liquids upon CO₂ adsorption. Therefore, we have calculated density, and volume expansion, $\Delta V/V \%$, defined according to the Gallagher et al.⁵⁹ criteria, eq 3

$$\frac{\Delta V}{V} \% = \frac{V_L(T, P, x) - V_1(T, P_0)}{V_1(T, P_0)} \times 100 \quad (3)$$

where V_L stands for the total volume of the ionic liquid with absorbed CO₂ at a given temperature and pressure, and V_1 for the total volume of the pure ionic liquid at the same temperature and 0.1 MPa pressure. Results are reported in Figure 15. Density values for [SA][CH] + CO₂ systems are larger than those for [BE][CH] + CO₂ systems in the studied composition range. Nevertheless, density evolves in an almost parallel way with mixture mole fraction for [BE][CH] and [SA][CH]. Likewise, the evolution of density with mixture composition shows two well-defined regions separated by x_{CO_2}

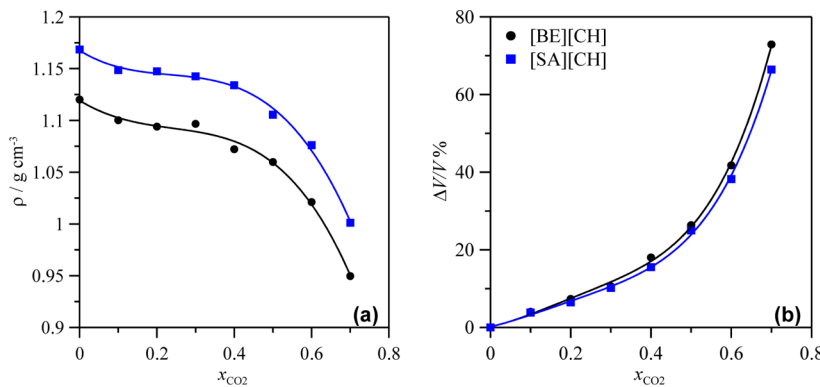


Figure 15. (a) Density, ρ , and (b) volume expansion, $\Delta V/V \%$, for $\text{CO}_2 +$ ionic liquid mixtures as a function of CO_2 mole fraction, x_{CO_2} , at 328 K obtained from molecular dynamic simulations. The corresponding pressures for each mixture are reported in Table S1 (Supporting Information).

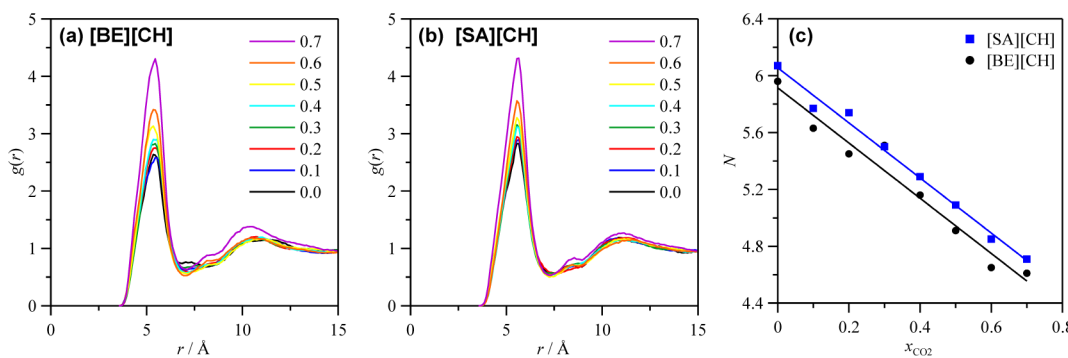


Figure 16. (a,b) Anion–cation center of mass radial distribution functions, $g(r)$, for $\text{CO}_2 + [\text{BE}][\text{CH}]$ and $\text{CO}_2 + [\text{SA}][\text{CH}]$, as a function of absorbed CO_2 mole fraction, and (c) corresponding running integrals, N , at 328 K, 0.1 MPa obtained from molecular dynamic simulations. Numeric values inside panels a and b show CO_2 mole fraction. Lines in panel c show linear fits for guiding purposes.

= 0.4, and thus, density decreases 4 and 3% on going from pure ionic liquids to 0.4 CO₂ mole fraction for [BE][CH] and [SA][CH], respectively, whereas on going from 0.4 to 0.7 CO₂ mole fraction density decreases 12%. Volume expansion is reported in Figure 15a, showing very small differences between both ionic liquids. The swelling effect of CO₂ on [BE][CH] and [SA][CH] is larger than those for common families of ionic liquids,^{16,58,60} moreover, if we compare our previous results for [LACTATE][CH],²⁹ we obtain $[\text{LACTATE}]^- < [\text{BE}]^- \approx [\text{SA}]^-$ for the $\Delta V/V \%$ ordering with the common [CH]⁺ cation. The simulated volumetric properties led to negative excess molar volumes, V_m^E , which were calculated using CO₂ supercritical molar volume at 328 K/7.400 MPa (246.52 cm³ mol⁻¹)⁶¹ to obtain values that could be compared with liquid values. Therefore, the estimated V_m^E values are -11.3 and -8.3 cm³ mol⁻¹ for [BE][CH] and [SA][CH], respectively, both for $x_{\text{CO}_2} = 0.5$. These large negative excess molar volumes are in agreement with values reported for other families of ionic liquids, Shiflett and Yokozeki⁶² reported a maximum V_m^E of -15 cm³ mol⁻¹ for equimolar mixtures of 1-butyl-methylimidazolium hexafluorophosphate with CO₂, and Shi and Maginn⁶³ reported values up to -45 cm³ mol⁻¹ for 1-hexyl-3-methylimidazolium bis(trifluoromethylsulfonyl)imide + CO₂ mixtures, whereas we reported for [LACTATE][CH] + CO₂ systems -10.5 cm³ mol⁻¹.²⁹

Microstructural features were analyzed using RDFs as a function of CO₂ mole fraction. The available experimental and computational studies on common families of ionic liquids have showed the almost negligible effect of absorbed CO₂ on ionic liquids structuring, which is showed by the weak effect on ion–

ion RDFs.^{60,64} We report in Figure 16 the changes of anion–cation center-of-mass RDFs with increasing CO₂ mole fraction. The position of the anion–cation RDFs peaks do not change with increasing CO₂ mole fraction on going from pure ionic liquids to mixtures with 0.7 CO₂ mole fraction the number of ions surrounding a counterion decreases in a linear way leading to just a 23% decrease. Results reported in Figure 16 show a very weak effect of absorbed CO₂ molecules on interionic interactions; ions seem to stay at almost the same distance even for very high CO₂ concentrations. RDFs for anion–CO₂ and cation–CO₂ were calculated to infer if CO₂ shows any preferential interaction, Figure 17. Reported results show very different shapes for ion–CO₂ RDFs; a wide band with maxima at 4.65 Å is obtained for anion–CO₂, whereas a sharp peak, with maxima at 5.45 Å, appears for cation–CO₂. Therefore, CO₂ molecules interact closely with [BE]⁻ and [SA]⁻ anions in comparison with [CH]⁺, nevertheless, interaction around the cation is also important. A more detailed picture of CO₂ interaction with involved ions may be inferred from SDFs, Figure 18. The comparison of results reported in Figures 9 and 18 show that the distribution of each ion around the corresponding counterions does not change with the absorption of CO₂ molecules. SDFs reported in Figure 18 show that CO₂ molecules occupy regions around anions and cations not occupied by the corresponding counterions, therefore, CO₂ molecules do not compete with ions around the corresponding counterion, and thus they occupy available free volume. The distribution of CO₂ molecules around anions is characterized by two strong caps on the top and bottom of the aromatic rings, and weaker caps in the sides of the ring. The

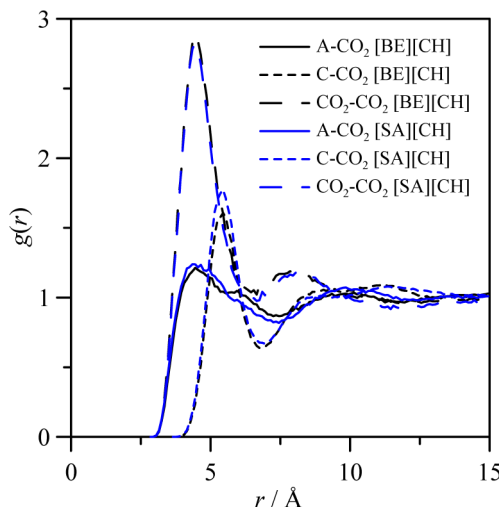


Figure 17. Ion–CO₂ and CO₂–CO₂ RDFs for CO₂ + [BE][CH] and CO₂ + [SA][CH] mixtures for $x_{\text{CO}_2} = 0.5$ at 328 K, 0.1 MPa, obtained from molecular dynamic simulations. A stands for anion and C stands for cation.

introduction of hydroxyl group in the anion weakens the CO₂ interaction with the anion in the ring side occupied by this hydroxyl group, but the remaining interactions do not change remarkably. The CO₂–cation interaction is characterized by a strong cap above the cation hydroxyl group and weaker caps on the sides of [CH]⁺ cation, these side CO₂–cation interactions are reinforced on going from [BE][CH] to [SA][CH].

Interaction energies between CO₂ molecules and ions are of interest to characterize the behavior of the mixed systems, detailed info of all the terms is reported in Table S3 (Supporting Information), whereas the most remarkable features are included in Figure 19.⁶⁵ The effect of absorbed CO₂ on ion–ion interaction energies are reported in Figure 19a, energies for all the ionic pairs decrease (in absolute value) with increasing CO₂ mole fraction following a linear trend and in an almost parallel way for both ionic liquids. Nevertheless, ion–ion interaction energies decreases in the range 19–26% on

going from pure ionic liquids to $x_{\text{CO}_2} = 0.7$ with slightly larger decreases for [SA][CH] than for [BE][CH], which is in agreement with the structural effects reported in previous sections. Anion–CO₂ interaction energies are lower in absolute value than those for cation–CO₂ interaction, Figure 19b. We should note the very large anion–CO₂ interaction energies for [SA][CH] for low CO₂ concentrations, which point to very effective interactions for that composition range in comparison with [BE][CH]. Likewise, cation–CO₂ interaction energy evolves through a minimum in absolute value for both ionic liquids. CO₂–CO₂ interaction energy increases in a linear way with increasing CO₂ concentration. Therefore, the behavior of both ionic liquids is very similar, which is in agreement with the reported structural behavior and CO₂ solubility. The hydroxyl group in [SA][−] anion increases the affinity of anion for CO₂ molecules and also the affinity of [CH]⁺ cation for CO₂ molecules, although the differences are also remarkable for low CO₂ mole fractions. Therefore, results reported in Figure 19 points to slightly stronger affinity of [SA][CH] than [BE][CH] for CO₂ molecules, but effects rising from the volume are more favorable for [BE][CH] than for [SA][CH], and thus the balance between volumetric and interaction energy effects determine the CO₂ solubility in the studied ionic liquids.

A very important feature on the study of ionic liquid + CO₂ mixed systems is the behavior of the dynamic properties upon mixing, which is especially important for very viscous ionic liquids such as those studied in this work. Ahosseini et al.⁶⁶ measured the variation of dynamic viscosity with increasing CO₂ concentration for several classical imidazolium-based ionic liquids, and their reported results showed a remarkable viscosity decrease upon CO₂ absorption, which was justified considering the decrease of intermolecular forces with increasing CO₂ concentration. Nevertheless, this effect was less important with increasing temperature. In a previous study, we reported the dynamic properties of [LACTATE][CH] ionic liquid mixed with CO₂,²⁹ the results showed increasing self-diffusion coefficients with increasing CO₂ mole fraction, with strong effects in the 0–0.1 CO₂ mole fraction range, and thus,

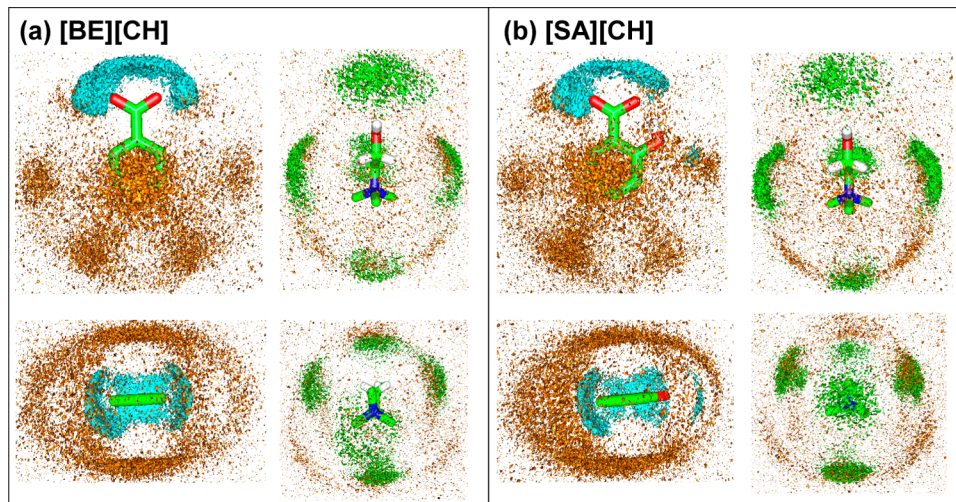


Figure 18. Relevant spatial distribution functions for (a) CO₂ + [BE][CH] and (b) CO₂ + [SA][CH] mixtures for $x_{\text{CO}_2} = 0.5$ at 328 K, 0.1 MPa, obtained from molecular dynamic simulations. Color code: (cyan, 15 times bulk density), hydroxyl hydrogens in [CH]⁺ cations (H4 atoms, Figure 8) around anions; (green, 15 times bulk density), C5 atoms in anions (Figure 8) around cations; (orange, 10 times bulk density), C in CO₂ around anion or cation. Top and bottom rows show different perspectives of the same SDFs.

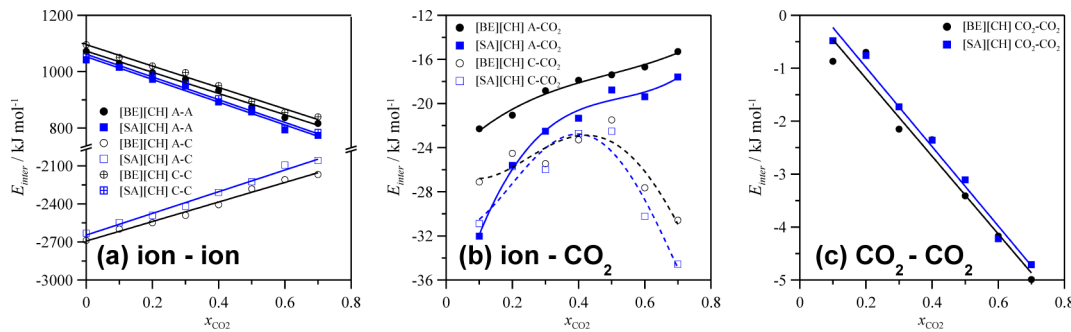


Figure 19. Intermolecular interaction energies, sum of Lennard-Jones and electrostatic contributions, for $\text{CO}_2 + [\text{BE}][\text{CH}]$ and $\text{CO}_2 + [\text{SA}][\text{CH}]$, as a function of CO_2 mole fraction, x_{CO_2} , obtained from molecular dynamics simulations at 328 K and 0.1 MPa. All values in kJ mol^{-1} . A stands for anion and C stands for cation. Lines show linear and polynomial fits for guiding purposes.

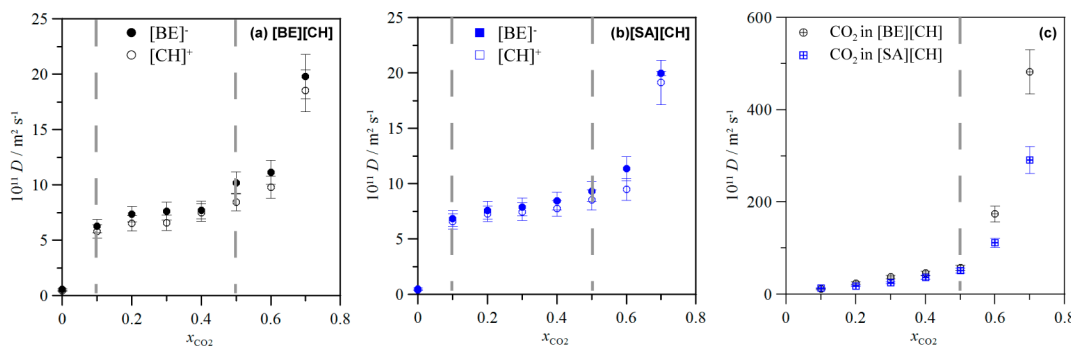


Figure 20. Self-diffusion coefficients, D , for $\text{CO}_2 + [\text{BE}][\text{CH}]$ and $\text{CO}_2 + [\text{SA}][\text{CH}]$, as a function of CO_2 mole fraction, x_{CO_2} , obtained from molecular dynamics simulations at 328 K and 0.1 MPa. D values obtained from Einstein's relationship from mean square displacements. Dashed lines show the regions with different trends.

decreasing viscosity. We have calculated self-diffusion coefficients and dynamic viscosities for the mixed systems as a function of composition, Figures 20 and 21. The studied

increasing CO_2 mole fraction. The evolution of self-diffusion coefficients with increasing CO_2 concentration show the following three regions, Figure 20a,b: (i) from pure ionic liquids to 0.1 CO_2 mole fraction, D values increases in an abrupt way, (ii) in the 0.1 to 0.5 range, D values increases in an almost linear way very slowly, and (iii) for CO_2 mole fraction larger than 0.5, all D values increases in an abrupt way. These results can not be explained considering the evolution of intermolecular interaction energies reported in Figure 19, which showed almost linear variations. Likewise, the analysis reported in previous sections showed that CO_2 molecules does not changes remarkably the anion–cation interactions as the almost constant characteristics of RDFs and SDFs showed. The most suitable explanation rises from the rearrangement of available void spaces to fit CO_2 molecules, which seem to favor the molecular mobility; this fact would lead to the behavior reported in the 0 to 0.1 CO_2 mole fraction region. In the 0.1 to 0.5 CO_2 mole fraction region, transitional behavior, void spaces are occupied by increasing quantities of CO_2 molecules without remarkable changes in the dynamic properties. For CO_2 mole fractions larger than 0.5, fluids show CO_2 -like behavior, CO_2 molecules control the mixed fluids structuring, and thus, self-diffusion coefficients increases remarkably. The calculated dynamic viscosity, Figure 21, shows an analogous behavior: increasing CO_2 mole fraction decreases remarkably the fluid's viscosity but changes with the amount of absorbed CO_2 are clearly nonlinear. Likewise, the rearrangement of void spaces with increasing CO_2 mole fraction allow increasing CO_2 molecules clustering with each other. This increasing CO_2-CO_2 clustering is clearly inferred from density maps reported in Figure 22; for $x_{\text{CO}_2} > 0.5$, large domains of CO_2 molecules are

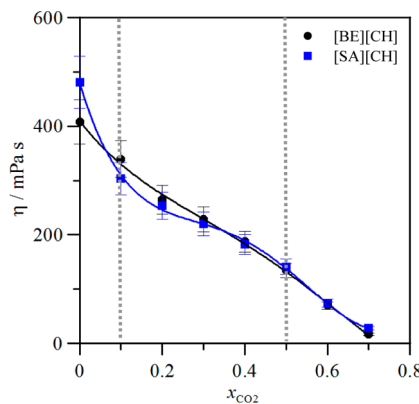


Figure 21. Dynamic viscosity, η , for $\text{CO}_2 + [\text{BE}][\text{CH}]$ and $\text{CO}_2 + [\text{SA}][\text{CH}]$, as a function of CO_2 mole fraction, x_{CO_2} , obtained from molecular dynamics simulations at 328 K and 0.1 MPa. η values obtained using the Green–Kubo method. Lines show polynomial fits for guiding purposes.

systems shows dynamic heterogeneity, which have been previously studied from theoretical^{52,53,67} and experimental viewpoints.^{68,69} Self-diffusion coefficients for CO_2 molecules are remarkably larger than those for ions, especially for large CO_2 mole fractions. Self-diffusion coefficients for anions are larger than those for cations for both ionic liquids, and both ionic liquids show similar values for both ions, and trends with

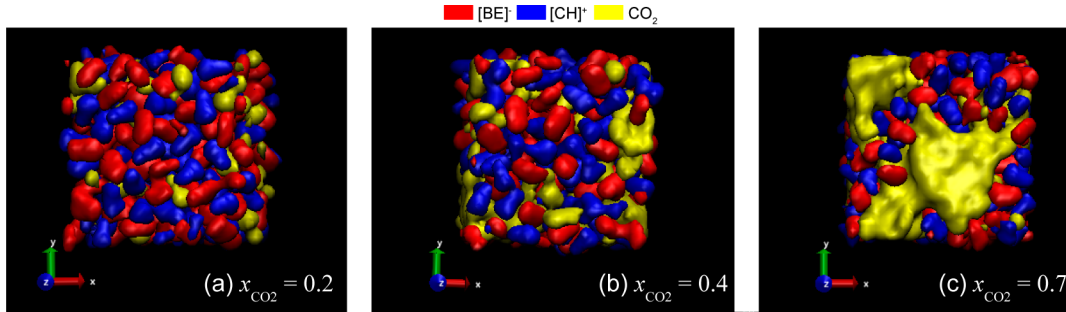


Figure 22. Number density maps for $\text{CO}_2 + [\text{BE}][\text{CH}]$ as a function of CO_2 mole fraction, x_{CO_2} , obtained from molecular dynamics simulations at 328 K and 0.1 MPa. Reported maps are obtained averaging 10 ns simulations.

obtained (CO_2 clusters with larger sizes), and for the larger mole fraction studied in this work ($x_{\text{CO}_2} = 0.7$, Figure 22c) fluids with large regions dominated by CO_2 clusters are obtained. This can be quantified with results reported in Figure 23 in which the number of CO_2 molecules surrounding a

group and the hydroxyl cationic group with less important interaction through the anion hydroxyl group for salicylate anion. CO_2 -ion pairs show moderate interactions, being stronger with the benzoate anion. AIM analysis allowed to infer the characteristics of all the interactions from a topological viewpoint and NBO approach allowed to analyze the strength of the interactions from the viewpoint of symmetry and energy differences between the donor and acceptor sites. Molecular dynamics simulations of pure and CO_2 -ionic liquid mixtures showed a very weak effect on the ionic liquid structuring upon CO_2 absorption, but with larger swelling effect than with other families of ionic liquids. Spatial distribution of CO_2 molecules rises from the rearrangement of available void spaces both around cations and anions, which occupy the same spatial regions than in pure ionic liquids, and thus, leading to a moderate weakening of ion-ion interactions. Likewise, CO_2 molecules and ions do not share regions around other ions; they occupy different regions, which do not overlap. The dynamic properties of pure ionic liquids show that cholinium-based ionic liquids with the studied aromatic cations have molecular mobilities remarkably lower, and thus, larger viscosities, than ionic liquids containing the same cation but nonaromatic ions such as lactate ones. This effect rises by the strength of intermolecular forces but also from steric reasons, nevertheless, the reported results discard the existence of anion-anion remarkable interaction, which could be used to justify the lower mobility through stacking effects. The adsorption of CO_2 molecules leads to highly heterogeneous systems from a dynamic viewpoint, with remarkable increase in molecular mobility, and decreasing viscosity. The changes of dynamic properties with increasing CO_2 mole fraction are clearly nonlinear with sudden changes for low mole fractions rising from the rearrangement of void space to fit CO_2 molecules, a further occupation of these void volumes, which does not change remarkably the dynamics of the studied systems, and thus evolving to a CO_2 -like fluid for large CO_2 mole fractions. The development of increasing CO_2 clustering with increasing CO_2 mole fraction is also inferred, leading to two well-defined regions (for compositions lower and larger than equimolar mole fractions) with very different structural and dynamic behavior.

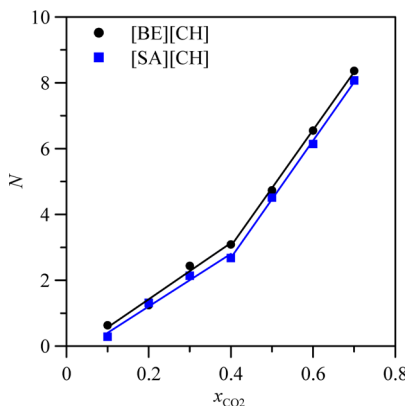


Figure 23. Number of CO_2 molecules surrounding a central CO_2 molecule for $r \leq 7.0 \text{ \AA}$ (first minimum in Figure 17 for CO_2-CO_2 RDFs) obtained from molecular dynamics simulations at 328 K and 0.1 MPa. Lines show linear fits.

central CO_2 molecule are reported for distances lower than 7.0 Å (the first minima for CO_2-CO_2 RDFs in Figure 17). Results reported in Figure 23 show two regions of clearly different behavior for the low CO_2 mole fraction region the number of CO_2 molecules surrounding a central CO_2 increases linearly with CO_2 concentration, whereas for the high mole fraction region a sudden change in the slope is obtained, which points to the development of large CO_2 clusters in agreement with results reported in Figure 23. This behavior will also justify the evolution in volumetric properties with CO_2 concentration reported in Figure 15. Likewise, the increasing CO_2 cluster sizing would improve improve the fluid dynamics sharply at high CO_2 concentrations, as reported in Figures 20 and 21.

4. CONCLUSIONS

A computational study on the molecular level behavior of cholinium-based ionic liquids combined with aromatic anions, pure and mixed with CO_2 , was performed for the very first time. The suitable environmental and toxicological properties of these fluids, together with the poor understanding of their microscopic properties required this study. Quantum chemistry analysis of short-range anion-cation interactions showed that interionic interactions is developed between the COO anionic

ASSOCIATED CONTENT

S Supporting Information

Table S1 (systems and conditions used for molecular dynamics simulations), Table S2 (force field parameters for $[\text{CH}]^+$ cation, $[\text{BE}]^-$ and $[\text{SA}]^-$ anions, and CO_2 molecule, Figure S1 (structures for $[\text{SA}][\text{CH}]$ ionic pair interacting through the methyl groups in $[\text{CH}]^+$), Figure S2 (structures for $[\text{SA}][\text{CH}]$

ionic pair interacting through the hydroxyl groups), Figure S3 (MK charges for the ionic pairs), Figure S4 (evolution of systems' potential energy as a function of simulation time), Table S3 (intermolecular interaction energies for CO₂ + ionic liquid systems). This material is available free of charge via the Internet at <http://pubs.acs.org>.

AUTHOR INFORMATION

Corresponding Author

*E-mail: sapar@ubu.es.

Notes

The authors declare no competing financial interest.

ACKNOWLEDGMENTS

Authors acknowledge the financial support by Ministerio de Ciencia e Innovación, Spain, (Project CTQ2010-15871) and from NPRP Grant (NPRP-09-739-2-284) from the Qatar National Research Fund.

REFERENCES

- (1) Castner, E. W.; Margulis, C. J.; Maroncelli, M.; Wishart, J. F. *Annu. Rev. Phys. Chem.* **2011**, *62*, 85–105.
- (2) Werner, S.; Haumann, M.; Wasserscheid, P. *Ann. Rev. Chem. Biochem. Eng.* **2010**, *1*, 203–230.
- (3) *Ionic liquids: Theory, Properties, New Approaches*; Kokorin, A., Ed.; InTech: Rijeka, Croatia, 2011.
- (4) Castner, E. W.; Wishart, J. F. *J. Chem. Phys.* **2010**, *132*, 120901–1–120901–8.
- (5) Davis, J. H. *Chem. Lett.* **2004**, *33*, 1072–1077.
- (6) Giernoth, R. *Angew. Chem., Int. Ed.* **2010**, *49*, 2834–2839.
- (7) Gurkan, B.; Goodrich, B. F.; Mindrup, E. M.; Ficke, L. E.; Masse, M.; Seo, S.; Senftle, T. P.; Wu, H.; Glaser, M. F.; Shah, J. K.; Maginn, E. J.; Brennecke, J. F.; Schneider, W. F. *J. Phys. Chem. Lett.* **2010**, *1*, 3494–3499.
- (8) Ueno, K.; Tokuda, H.; Watanabe, M. *Phys. Chem. Chem. Phys.* **2010**, *12*, 1649–1658.
- (9) Bernard, U. L.; Izgorodina, E. L.; MacFarlane, D. R. *J. Phys. Chem. C* **2010**, *114*, 20472–20478.
- (10) Fumino, K.; Wulf, A.; Verevkin, S. P.; Heintz, A.; Ludwig, R. *Chem. Phys. Chem.* **2010**, *11*, 1623–1626.
- (11) Huang, J.; Rüther, T. *Aust. J. Chem.* **2009**, *62*, 298–308.
- (12) Karadas, F.; Atilhan, M.; Aparicio, S. *Energy Fuels* **2010**, *24*, 5817–5828.
- (13) Yang, Z. Z.; Zhao, Y. N.; He, L. N. *RSC Adv.* **2011**, *1*, 545–567.
- (14) Hu, Y. F.; Liu, Z. C.; Xu, C. M.; Ming, X. *Chem. Soc. Rev.* **2011**, *40*, 3802–3823.
- (15) Huang, X.; Margulis, C. J.; Li, M.; Berne, B. J. *J. Am. Chem. Soc.* **2005**, *127*, 17842–17851.
- (16) Babarao, R.; Dai, S.; Jiang, D. *J. Phys. Chem. B* **2011**, *115*, 9789–9794.
- (17) Aparicio, S.; Atilhan, M.; Karadas, F. *Ind. Eng. Chem. Res.* **2010**, *49*, 9580–9595.
- (18) Scammells, P.; Scott, J.; Singer, R. D. *Aust. J. Chem.* **2005**, *58*, 155–169.
- (19) Petkovic, M.; Seddon, K.; Rebelo, L. P. N.; Silva, C. *Chem. Soc. Rev.* **2011**, *40*, 1383–1403.
- (20) Yu, Y.; Lu, X.; Zhou, Q.; Dong, K.; Yao, H.; Zhang, S. *Chem.—Eur. J.* **2008**, *14*, 11174–11182.
- (21) Petkovic, M.; Ferguson, J. L.; Nimal, H. Q.; Ferreira, R.; Leitao, M. C.; Seddon, K. R.; Silva, C. *Green Chem.* **2010**, *12*, 643–649.
- (22) Costa, A. J. L.; Soromenho, M. R. C.; Shimizu, K.; Marrucho, I. M.; Esperanca, J. M. S. S.; Canongia, J. N.; Rebelo, L. P. N. *Chem. Phys. Chem.* **2012**, *13*, 1902–1909.
- (23) Maginn, E. J. *Phys.: Condens. Matter* **2009**, *21*, 373101.
- (24) Roth, C.; Appelhagen, A. *Chem. Phys. Chem.* **2012**, *13*, 1708–1717.
- (25) Sun, H.; Zhang, D.; Liu, C. *J. Phys. Chem. A* **2010**, *114*, 3990–3996.
- (26) Zhang, Y.; Chen, X. Y.; Wang, H. J.; Diao, K. S.; Chen, J. M. *J. Mol. Struc. Theochem.* **2010**, *952*, 16–24.
- (27) Aparicio, S.; Atilhan, M. *Energy Fuels* **2011**, *24*, 4989–5001.
- (28) Aparicio, S.; Alcalde, R.; Atilhan, M. *J. Phys. Chem. B* **2010**, *114*, 5795–5809.
- (29) Aparicio, S.; Atilhan, M.; Khraisheh, M.; Alcalde, R. *J. Phys. Chem. B* **2011**, *115*, 12473–12486.
- (30) Swatlowski, R. P.; Holbrey, J. D.; Rogers, R. D. *Green Chem.* **2003**, *5*, 361–363.
- (31) Wood, N.; Stephens, G. *Phys. Chem. Chem. Phys.* **2010**, *12*, 1670–1674.
- (32) Frisch, M. J.; Trucks, G. W.; Schlegel, H. B.; Scuseria, G. E.; Robb, M. A.; Cheeseman, J. R.; Montgomery, Jr., J. A.; Vreven, T.; Kudin, K. N.; Burant, J. C. et al. *Gaussian 03*, Revision C.02; Gaussian, Inc.: Wallingford, CT, 2004.
- (33) Becke, A. D. *Phys. Rev. A* **1988**, *38*, 3098–3100.
- (34) Lee, C.; Yang, W.; Parr, R. G. *Phys. Rev. B* **1988**, *37*, 785–789.
- (35) Becke, A. D. *J. Chem. Phys.* **1993**, *98*, 5648–5652.
- (36) Singh, U. C.; Kollman, P. A. *J. Comput. Chem.* **1984**, *5*, 129–145.
- (37) Besler, B. H.; Merz, K. M.; Kollman, P. A. *J. Comput. Chem.* **1990**, *11*, 431–439.
- (38) Simon, S.; Duran, M.; Dannenberg, J. J. *J. Chem. Phys.* **1996**, *105*, 11024–11031.
- (39) Bader, R. F. W. *Atoms in Molecules: A Quantum Theory*; Oxford University Press: Oxford, 1990.
- (40) Biegler-König, F.; Schönbohm, J.; Bayles, D. *J. Comput. Chem.* **2001**, *22*, 545–559.
- (41) Reed, A. E.; Curtiss, L. A.; Weinhold, F. *Chem. Rev.* **1988**, *88*, 899–926.
- (42) Eckert, F.; Klamt, A. *COSMOthermX*, Version C21_0111; COSMOlogic GmbH & Co. KG: Leverkusen, Germany, 2010.
- (43) Lyubartsev, A. P.; Laaksonen, A. *Comput. Phys. Commun.* **2000**, *128*, 565–589.
- (44) Hoover, W. G. *Phys. Rev. A* **1985**, *31*, 1695–1697.
- (45) Tuckerman, M.; Berne, B. J.; Martyna, G. J. *J. Chem. Phys.* **1992**, *97*, 1990–2001.
- (46) Essmann, U. L.; Perera, M. L.; Berkowitz, T.; Darden, H.; Lee, H.; Pedersen, L. G. *J. Chem. Phys.* **1995**, *103*, 8577–8593.
- (47) Van-Oanh, N. T.; Houriez, C.; Rousseau, B. *Phys. Chem. Chem. Phys.* **2010**, *12*, 930–936.
- (48) Chen, T.; Chidambaram, M.; Liu, Z.; Smit, B.; Bell, A. T. *J. Phys. Chem. B* **2010**, *114*, 5790–5794.
- (49) Chaban, V. V.; Voroshilova, I. V.; Kalugin, O. N. *Phys. Chem. Chem. Phys.* **2011**, *13*, 7910–7920.
- (50) Margulis, C. J. *Mol. Phys.* **2004**, *102*, 829–838.
- (51) Shannon, M. S.; Tedstone, J. M.; Danielsen, S. P. O.; Hindman, M. S.; Irvin, A. C.; Bara, J. E. *Ind. Eng. Chem. Res.* **2012**, *51*, 5565–5576.
- (52) Del-Popolo, M. G.; Voth, G. A. *J. Phys. Chem. B* **2004**, *108*, 1744–1752.
- (53) Hu, Z.; Margulis, C. *Proc. Natl. Acad. Sci. U.S.A.* **2006**, *103*, 831–836.
- (54) Zhang, X.; Liu, Z.; Wang, W. *AIChE J.* **2008**, *54*, 2717–2728.
- (55) Maiti, A. *ChemSusChem* **2009**, *2*, 628–631.
- (56) Ab-Manan, N.; Hardrake, C.; Jacquemin, J.; Rooney, D. W.; Youngs, T. G. A. *J. Chem. Eng. Data* **2009**, *54*, 2005–2022.
- (57) Huang, X.; Margulis, C. J.; Li, Y.; Berne, B. J. *J. Am. Chem. Soc.* **2005**, *127*, 17842–17851.
- (58) Aki, S. N. V. K.; Mellein, B. R.; Saurer, E. M.; Brennecke, J. F. *J. Phys. Chem. Soc.* **2004**, *108*, 20355–20365.
- (59) Gallagher, P. M.; Coffey, M. P.; Krukonis, V. J.; Klasutis, N. In *Supercritical Fluid Science and Technology*; Johnson, K. P., Penninger, J. M. L., Eds.; ACS Symposium Series 406; American Chemical Society: Washington, DC, 1989; pp 334–354.
- (60) Bhargava, B. L.; Krishna, A. C.; Balasubramanian, S. *AIChE J.* **2008**, *54*, 2971–2978.

- (61) Lemmon, E. W.; Huber, M. L.; McLinden, M. O. REFPROP. Reference Fluid Thermodynamic and Transport Properties. *NIST Standard Reference Database 23*, Version 9.0; U.S. Secretary of Commerce: Washington, DC, 2010.
- (62) Shiflett, M. B.; Yokozeki, A. *J. Phys. Chem. B* **2006**, *110*, 14436–14443.
- (63) Shi, W.; Maginn, E. *J. Phys. Chem. B* **2008**, *112*, 2045–2055.
- (64) Cadena, C.; Anthony, J. L.; Shah, J. K.; Morrow, T. I.; Brennecke, J. F.; Maginn, E. *J. Am. Chem. Soc.* **2004**, *126*, 5300–5308.
- (65) Shi, W.; Sorescu, D. C.; Luebke, D. R.; Keller, M. J.; Wickramanayake, S. *J. Phys. Chem.* **2010**, *114*, 6531–6541.
- (66) Ahosseini, A.; Ortega, E.; Scurto, A. M. *Fluid Phase Equilib.* **2009**, *286*, 72–78.
- (67) Yan, T.; Wang, Y.; Knox, C. *J. Phys. Chem. B* **2010**, *114*, 6866–6904.
- (68) Burrell, G. L.; Burgar, I. M.; Gong, Q. *J. Phys. Chem. B* **2010**, *114*, 11436–11443.
- (69) Castigliones, F.; Raos, G.; Appetecchi, G. B.; Montanino, M.; Passerini, S.; Moreno, M.; Famulari, A.; Mele, A. *Phys. Chem. Chem. Phys.* **2010**, *12*, 1784–1792.